ARTICLE

Band-Order Anomaly at the γ-Al$_2$O$_3$/SrTiO$_3$ Interface Drives the Electron-Mobility Boost

Alla Chikina, Dennis V. Christensen, Vladislav Borisov, Marius-Adrian Husanu, Yunzhong Chen, Xiaoqiang Wang, Thorsten Schmitt, Milan Radovic, Naoto Nagaosa, Andrey S. Mishchenko, Roser Valentí, Nini Pryds,* and Vladimir N. Strocov*

Cite This: *ACS Nano* 2021, 15, 4347−4356

Read Online

ACCESS | Metrics & More | Article Recommendations | SI Supporting Information

ABSTRACT: The rich functionalities of transition-metal oxides and their interfaces bear an enormous technological potential. Its realization in practical devices requires, however, a significant improvement of yet relatively low electron mobility in oxide materials. Recently, a mobility boost of about 2 orders of magnitude has been demonstrated at the spinel−perovskite γ-Al$_2$O$_3$/SrTiO$_3$ interface compared to the paradigm perovskite−perovskite LaAlO$_3$/SrTiO$_3$ interface. We explore the fundamental physics behind this phenomenon from direct measurements of the momentum-resolved electronic structure of this interface using resonant soft-X-ray angle-resolved photoemission. We find an anomaly in orbital ordering of the mobile electrons in γ-Al$_2$O$_3$/SrTiO$_3$ which depopulates electron states in the top SrTiO$_3$ layer. This rearrangement of the mobile electron system pushes the electron density away from the interface, which reduces its overlap with the interfacial defects and weakens the

electron−phonon interaction, both effects contributing to the mobility boost. A crystal-field analysis shows that the band order alters owing to the symmetry breaking between the spinel γ-Al$_2$O$_3$ and perovskite SrTiO$_3$. Band-order engineering, exploiting the fundamental symmetry properties, emerges as another route to boost the performance of oxide devices.

KEYWORDS: transition-metal oxides, heterostructures, photoelectron spectroscopy, electronic band structure, electron−phonon interactions
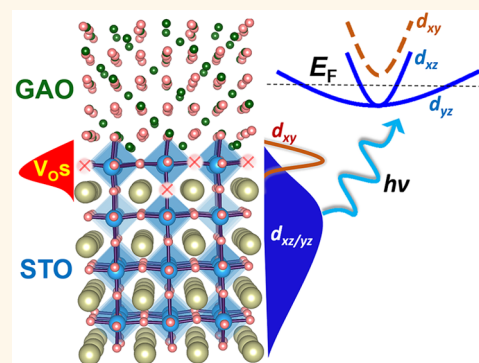
The rich interplay of spin, orbital, and lattice degrees of freedom in transition-metal oxides (TMOs) results in a variety of unconventional phenomena, ranging from superconductivity to ferroelectricity, colossal magnetoresistance, and ferromagnetism, which can be further enriched by interfacing these materials. A paradigm example is the two-dimensional electron system (2DES) that can spontaneously form at the interface between two perovskite band insulators, LaAlO$_3$ (LAO) and SrTiO$_3$ (STO); for reviews, see refs 1 and 2. This interface combines many intriguing and even mutually exclusive properties, such as superconductivity and ferromagnetism.[3] Field-effect tunability of these properties[2,4] allows realization of superconducting field-effect transistors and switchable magnetic states. Whereas the electron concentration (n_s) accumulated by the TMO interfaces is typically a couple of orders of magnitude larger than that at the semiconductor interfaces, the electron mobility (μ_e) still stays a few orders of magnitude less.[5] In order to bring the functionality of the TMO interfaces to a level adequate for high-performance practical devices, this fundamental electron transport characteristic needs to be much improved. The limiting factors here include defect scattering, electron-correlation phenomena, and, for the STO-based interfaces in particular, a strong electron−

phonon interaction (EPI), resulting in the polaronic nature of the interfacial charge carriers.[6]

Different routes to increase μ_e of the TMO systems can be envisaged. The most common one is the so-called defect engineering, where the sample preparation procedure is tuned to reduce the concentration of defect scattering sites, including the oxygen vacancies (V$_O$s), or, in the spirit of the semiconductor high-electron-mobility transistors (HEMTs),[7,8] to shift their distribution away from the itinerant electrons. An example of such an approach is a modulation-doped heterostructure where a LaMnO$_3$ buffer layer is inserted between amorphous LAO and STO,[9] which not only reduces the concentration of V$_O$s on the STO side but also serves as a spacer to increase the spatial separation between the electrons and the scattering sites.
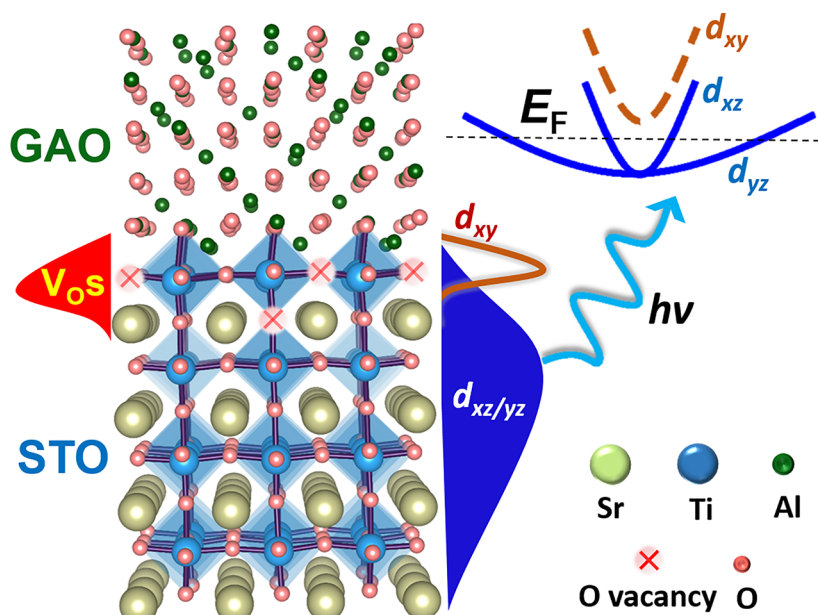
Figure 1. Scheme of the GAO/STO interface probed with k-resolved photoemission to directly image electron dispersions. The ARPES experiment finds the band-order anomaly $d_{xy} > d_{xz}/d_{yz}$ which promotes spatial separation of the V_Os from the 2DES to boost μ_e.

Recently, the epitaxial heterostructure of spinel γ-Al$_2$O$_3$ (GAO) deposited on perovskite STO was found to exhibit extremely high μ_e values of up to 140 000 cm^2/(V·s), compared to around 1000 cm^2/(V·s) in a typical LAO/STO heterostructure.[10] This qualifies GAO/STO as the highest-μ_e TMO system after the ZnO-based ones.[11] Understanding the fundamental physics behind this μ_e-boost will be extremely important for further progress of the TMO-based devices. A recent photoemission study of GAO/STO supported by first-principles calculations[12] suggested an efficient diffusion of V_Os from the STO bulk to the interface, reducing defect scattering of electrons deeper in STO. However, as the lowest-energy electron states in typical STO-based heterostructures are the d_{xy} ones located in the V_O-rich top TiO$_2$ layer,[4,13] it remained unclear why the d_{xy} electrons did not impair the overall μ_e. Intriguingly, later X-ray linear dichroism (XLD) experiments at the Ti 2p absorption edge[14,15] suggested a change in the band order in GAO/STO heterostructures, where the d_{xy} states shift above the d_{xz}/d_{yz} ones, in contrast to the usual $d_{xz}/d_{yz} > d_{xy}$ band order at most STO-based interfaces. However, those experiments could not determine the **k**-resolved band structure of the 2DES, and, most importantly, they probed only the unoccupied states not directly involved in electron transport. Furthermore, the driving force of such a band-order anomaly and its connection with the μ_e-boost stayed unclear.

Here, we explore the factors of the μ_e-boost in GAO/STO from direct measurements of the **k**-resolved electronic structure of the buried 2DES, as schematized in Figure 1, using resonant soft-X-ray angle-resolved photoelectron spectroscopy (ARPES) at the Ti 2p edge. The experiment reveals an anomalous band order, where the d_{xy} band shifts above the d_{xz}/d_{yz} ones and depopulates. We reveal that this anomaly shifts the overall electron density away from the V_O-rich top STO layer, and the subsequent reduction of the effective defect concentration and the EPI strength, experienced by the mobile electrons, boosts μ_e. A crystal-field (CF) analysis for the interfacial Ti atoms shows that the band-order anomaly is caused by symmetry breaking at the non-isomorph spinel–

perovskite interface of GAO/STO. Our analysis puts forward a yet unexplored avenue of the band-order engineering using symmetry breaking to tune properties of the TMO heterostructures toward particular device functionalities.

RESULTS

The GAO/STO samples were grown by pulsed laser deposition (PLD) under different oxygen pressures, resulting in different n_s (see Methods).[16,17] We have investigated a sample having low $n_s \approx 3 \times 10^{13}$ cm^{-1} and $\mu_e \approx 12\,000$ cm^2/(V·s) at 2 K, and another one having high $n_s \approx 6 \times 10^{14}$ cm^{-2} and $\mu_e \approx 100\,000$ cm^2/(V·s) at 2 K, with such dramatic variations of n_s and μ_e being typical of STO-based systems. The simultaneous increase of n_s and μ_e is a hallmark of GAO/STO. Our soft-X-ray ARPES experiments (see Methods) focused on the fundamental electronic structure characteristics—Fermi surface (FS), band dispersions and band order, and spectral function—of the interfacial 2DES in these samples compared side-by-side with the paradigm LAO/STO interface irradiated by X-rays to create V_Os. Both systems are oxygen-deficient, with the V_Os concentrated in the top STO layer.[18,19] For more on the electronic structure of the localized V_O-derived in-gap (IG) states in GAO/STO see the Supporting Information (SI) and the references therein. To access the buried Ti t_{2g}-derived 2DES in our samples, we used resonant photoexcitation at the Ti L_3-edge at a photon energy ($h\nu$) of 460.4 eV. First, we will analyze band structure of the 2DES states in terms of electron orbitals.

k-Resolved Electronic Structure: Band-Order Anomaly. Figure 2a presents an experimental ARPES image of the band dispersions along the ΓX direction of the Brillouin zone for our LAO/STO sample, measured with s-polarized incident X-rays, selecting the antisymmetric d_{xy} and d_{yz} states. The out-of-plane d_{yz} states show their characteristic flat dispersion, whereas the in-plane d_{xy} one has only a minute cross-section at high excitation energies[20] and is visible mostly in the points where it hybridizes with the d_{yz} states. Figure 2b represents the ARPES data measured with p-polarized X-rays, selecting the
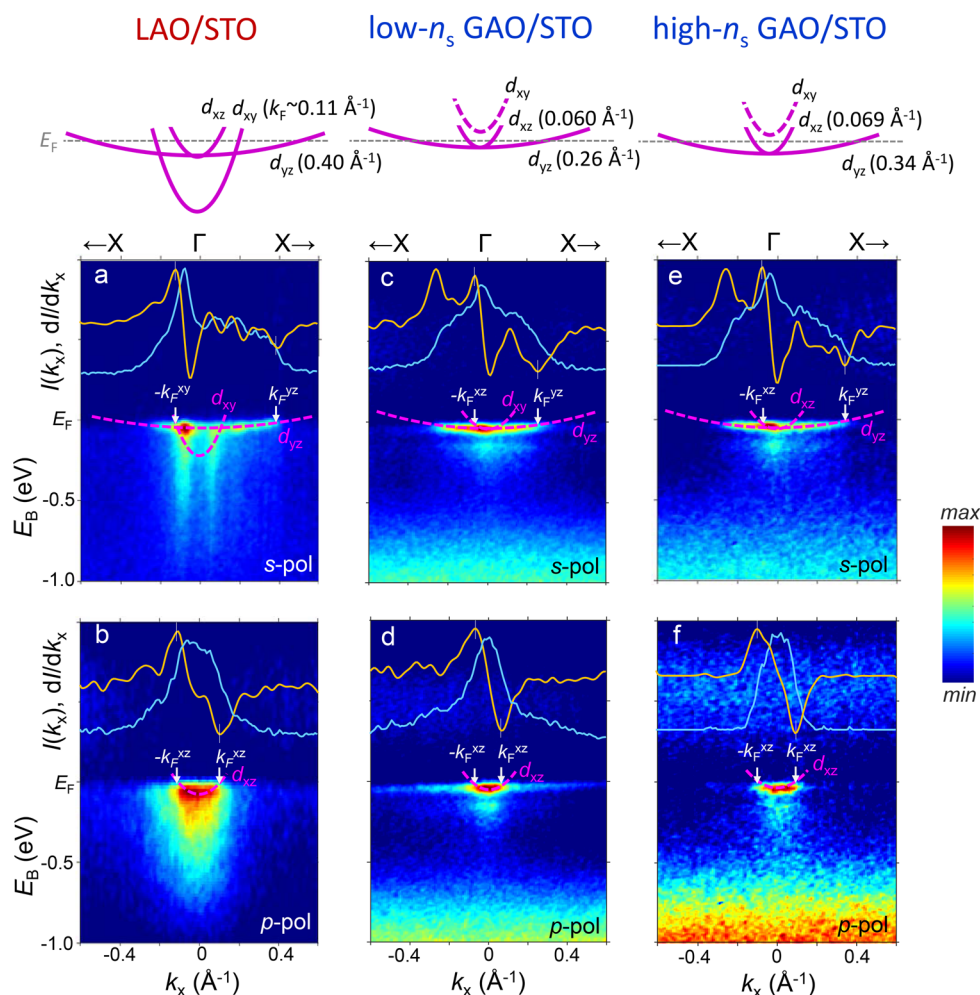
Figure 2. Experimental $E(k)$ images along ΓX for the oxygen-deficient LAO/STO interface (a,b) and low- and high-n_s GAO/STO interfaces (c,d and e,f, respectively) measured at $h\nu$ = 460.4 eV. For LAO/STO, s-polarized X-rays select the d_{xy} and d_{yz} bands (top panels) and p-polarized X-rays the d_{xz} bands (bottom panels), and for GAO/STO these selection rules relax. The momentum-distribution curves at E_F (cyan curves) and their gradients (yellow) are shown on top of each panel, with extremes of the latter (dashed lines) locating the k_F values (arrows). The sketches on top of the figure schematize the band order for the three samples, where GAO/STO shows the anomalous $d_{xy} > d_{xz}/d_{yz}$ band order with complete depopulation of the d_{xy} band.

symmetric d_{xz} states.[21,22] We note pronounced satellites below the band dispersions, identifying the polaronic nature of the interfacial charge carriers.[6,22]

Importantly, the experimental band structure of LAO/STO follows the $d_{xy} < d_{xz}/d_{yz}$ band order, with the d_{xy} band minimum shifted by ~200 meV below that of $d_{xz/yz}$.[19] Schematized on top of Figure 2a, such a pattern confirms the theoretical picture where the CF in bulk STO lowers the energy of Ti t_{2g} bands relative to the e_g ones, and interfacing STO with LAO further splits the former into the deeper d_{xy}-derived band and shallower d_{xz}/d_{yz} ones.[21–23] The d_{xy} states are located close to the interface, while the d_{xz}/d_{yz} ones extend into the STO bulk over a region of up to a few tens of nanometers, depending on the exact shape of the interfacial quantum well $V(r)$.[4,6,13] The $d_{xy} < d_{xz}/d_{yz}$ band order observed in LAO/STO is actually universal across a wide range of systems based on TiO_2-terminated STO, almost independent of the growth conditions and oxygen deficiency. It starts from the paradigm LAO/STO interface[21] and survives under amorphous overlayers of LAO,[24,25] Si,[26] and a variety of metals[27–29] on STO as well as for bare STO surfaces prepared under various conditions[30,31] and even reconstructed by

sputtering/annealing.[32] This band order can, though, be tuned by applying pressure[33] or changing crystallographic orientations,[34] although the latter also changes the $d_{xy}/d_{xz}/d_{yz}$ orbital orientation relative to the surface or interface.

For GAO/STO, the experimental band structure of the d_{xy} and d_{yz} states shown in Figure 2c,e for the low- and high-n_s samples, respectively, appears quite different from that for LAO/STO. First of all, the proximity of GAO breaks the four-fold symmetry of STO due to the interfacial Ti cations which neighbor the tetrahedrally coordinated Al cations. Due to the concomitant relaxation of the above selection rules, at the s-polarization we observe a certain weight of the d_{xz} band on top of the d_{yz} one (Figure 2c,e), and at the p-polarization a certain weight of the d_{yz} band on top of the d_{xz} one (Figure 2d,f). Most importantly, the d_{xy}–d_{yz} hybridization points characteristic of LAO/STO disappear, indicating the absence of the d_{xy} band, which has shifted above E_F and depopulated. This band structure pattern, schematized on top of the figure, identifies an anomalous $d_{xy} > d_{xz}/d_{yz}$ band order as opposed to the universal $d_{xy} < d_{xz}/d_{yz}$ one represented by the above LAO/STO. The intensity enhancement at the bottom of the GAO/STO images is due to the V_O-derived IG states (see the SI).
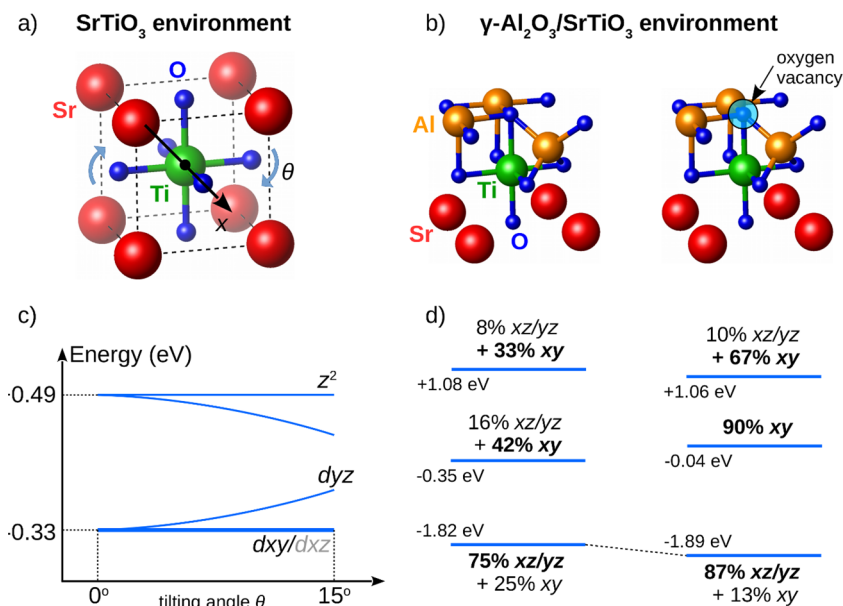
Figure 3. CF analysis for different atomic environments. (a) Structural sketch of bulk perovskite STO. (b) Structural sketch of one possible termination of the spinel−perovskite GAO/STO interface. (c) CF energy levels for bulk STO as a function of the oxygen octahedron's tilting angle. (d) Lowest CF energy levels for defect-free and oxygen-deficient GAO/STO environments, with the orbital character and weights indicated (the dominant weight in bold).

We note that the band order is associated with a small change of the effective mass of the d_{xz}/d_{yz} bands (see the SI), which, as we discuss later, can be related to the reduction of the EPI.

Therefore, our ARPES results reveal that electron transport in GAO/STO is exclusively due to the d_{xz}/d_{yz} electrons. We note that in many cases one can deduce the partial band occupancy from the non-linearity of the Hall coefficient as a function of magnetic field. In the case of high-mobility GAO/STO samples, however, the Hall coefficient shows a very pronounced anomalous Hall effect stemming from the magnetism, and the concomitant non-linearity hides possible multi-band effects. ARPES, in turn, clearly resolves the orbital character of the contributions to the total n_s.

We note that our ARPES findings of the anomalous band order in GAO/STO are consistent with the recent XLD experiments,[14,15] which are, though relevant for the band order in the unoccupied states, not directly related to the electron transport. Ionic liquid gating experiments[17] suggested the persistence of the universal band order in GAO/STO, but these experiments probe the band structure only indirectly and may be affected by electrochemical reactions.

The Fermi momenta (k_F) of the experimental bands, reflecting their population, were determined from the momentum-distribution curves (MDCs) of the ARPES intensity $I(k_x)$ integrated over the whole occupied energy width (W) of the bands (cyan lines in the band structure panels of Figure 2). The extremes of their gradient dI/dk_x (yellow lines) define the k_F values, indicated at the band schemes on top of Figure 2. We have utilized this gradient method, originally proposed by Straub et al.,[35] because in our case, where W is of the order of the experimental ΔE, the conventional determination of k_F from the maxima of the MDCs at E_F becomes obviously irrelevant. Assigning the dI/dk_x extremes to a particular k_F value, we should keep in mind that, at the negative-k_x side of the d_{yz} bands and positive-k_x side of the d_{xy} ones, the spectral intensity vanishes due to photoemission matrix elements. Inspecting the experimental

k_F, we observe that not only does the d_{xy} band depopulate when going from LAO/STO to GAO/STO, but also the d_{xz}/d_{yz} bands reduce their population; these bands increase their population between the low- to high-n_s GAO/STO samples. The relation of these observations with n_s and μ_e of the 2DES will be discussed later.

Symmetry-Breaking Origin of the Band-Order Anomaly. In order to get more insight into the origin of the band-order anomaly at the spinel−perovskite GAO/STO interface, we have theoretically analyzed the CF splitting effects in the ion-core regions of the interfacial Ti atoms. The CF potential was modeled for different atomic environments, depicted in Figure 3a,b. The point-charge approximation is used to calculate the spatial distribution of the electrostatic potential of N ions with nominal charges Q_i and coordinates r_i acting on electrons:

$$V_{CF}(r) = -\frac{1}{4\pi\varepsilon_0} \sum_{i=1}^{N} \frac{Q_i}{|r - r_i|}$$

The 3d states are approximated by the atomic orbitals with $n = 3$ and $l = 2$, which are used for evaluating the CF matrix:

$$\mathbf{H}_{CF} = \langle nlm_1|V_{CF}(r) - V_{CF}(0)|nlm_2\rangle$$

Here, $|nlm\rangle$ stands for spherical harmonics, and the values of m_1 and m_2 are between −2 and +2 and correspond to d_{z^2}, $d_{x^2-y^2}$, d_{xy}, d_{xz}, and d_{yz} orbitals. Diagonalization of the CF matrix $\mathbf{H}_{CF}$ gives information on the band ordering at the Γ-point for the selected atomic structure.

For the cubic STO atomic environment, Figure 3a, the d_{xy} vs d_{xz}/d_{yz} orbitals are degenerate. The degeneracy can be lifted, for example, by symmetry breaking when interfacing STO to other TMOs such as LAO, or by oxygen octahedra tilting. The latter, illustrated in Figure 3c, where the tilting around the x- or y-axes pushes the d_{yz} or d_{xz} states above the d_{xy} one, is typical of TMOs and constitutes one of the contributions to the interfacial potential in oxide heterostructures. The symmetry
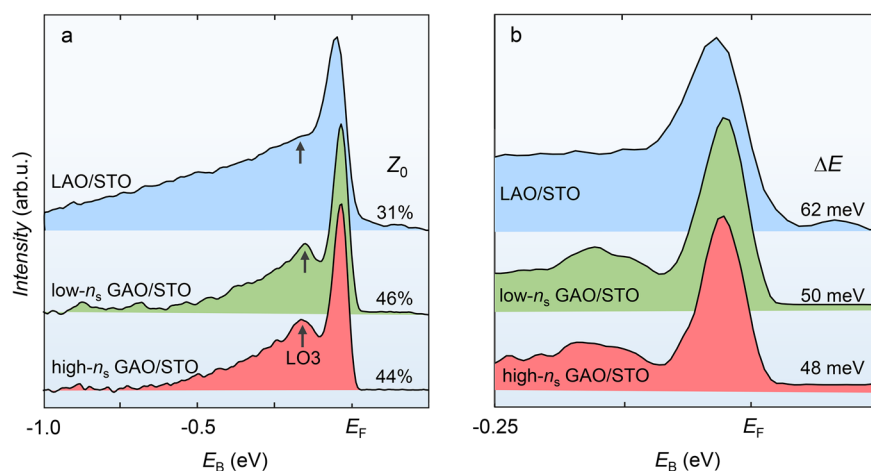
Figure 4. Experimental $A(\omega,\mathbf{k})$ for oxygen-deficient LAO/STO and two GAO/STO samples represented by EDCs of the ARPES intensity from Figure 2, integrated over (a) the whole $\pm k_F$ interval and (b) the $k_F \pm 0.1$ Å^{-1} interval. Compared to LAO/STO, in both GAO/STO samples the QP peak shows larger spectral weight Z_0 and smaller energy broadening ΔE (values on the plots), which identify weaker EPI and smaller effective disorder, respectively.

breaking and oxygen octahedra tilting both lead to a shift of the d_{xz}/d_{yz} orbitals above the d_{xy} one, Figure 3c, which was, indeed, commonly observed as the universal band order in numerous experimental and theoretical studies of STO-based interfaces.[19,21,36,37]

For the spinel–perovskite environment, Figure 3b, we find that the CF energy levels are dramatically rearranged due to the proximity of positively charged Al cations, which can be either octahedrally or tetrahedrally coordinated by oxygen. The particular coordination is crucial for the energy position of the IG states in GAO/STO formed by the V_Os but does not qualitatively change the anomalous band order of the metallic states, which stays inverse compared to that of LAO/STO. Our CF calculations suggest that the lowest energy level becomes dominated by the d_{xz}/d_{yz} states that are mixed in 1:1 ratio, while the next higher energy levels are mostly of the $+d_{xy}$ character, Figure 3d. We emphasize that this feature is robust with respect to whether the Al vacancies, intrinsically present in GAO, are located in the Al layer close to STO or elsewhere in GAO. In the studied example, the V_Os increase the energy separation between the d_{xy} and d_{xz}/d_{yz} orbitals slightly but do not change this picture qualitatively, simply providing electrons filling energy levels. Therefore, our analysis suggests that the band-order anomaly in GAO/STO originates from the different nature of the CF in the ion-core regions of the interfacial Ti atoms at this spinel–perovskite interface compared to the perovskite–perovskite LAO/STO one.

Spectral Function: Electron–Phonon Interactions and Disorder. We will now analyze another important ingredient of the electronic properties, the EPI, which is embedded in the spectral function $A(\omega,\mathbf{k})$ represented by the energy distribution curves (EDCs) of the ARPES intensity in Figure 2. Similarly to the previous analysis for the stoichiometric LAO/STO,[6,22] we will use $A(\omega)$ obtained by integration of $A(\omega,\mathbf{k})$ over the whole $\pm k_F$ interval of the d_{yz} bands. This approach allows full inclusion of the bosonic spectral satellites whose extension in $\mathbf{k}$-space may be narrower than the quasiparticle (QP) bands.[38] The experimental $A(\omega)$ values for our oxygen-deficient LAO/STO and both GAO/STO samples (where we subtracted the IG state weight protruding into the 2DES energy region) are presented in Figure 4a. Their pronounced peak–dip–hump line shape is a

hallmark of the strong EPI in STO-based systems, fundamentally reducing μ_e.[6,22] We recall that, whereas for LAO/STO the $A(\omega,\mathbf{k})$ reflects both d_{xy} and d_{xz}/d_{yz} states, for GAO/STO it reflects only the latter.

For LAO/STO, the hump is structureless and extends over a wide energy range, suggesting a continuum of phonon modes involved in the EPI. For GAO/STO, in contrast, the hump is a narrow peak separated from the QP one by ~100 meV, which corresponds to the LO3-phonon energy in STO.[32] The increase of the QP residual weight Z_0 from ~31% in LAO/STO to ~45% in GAO/STO signals a decrease of the EPI strength in the latter. Expectedly, this increase is associated with a notable reduction of the effective mass of the d_{xz}/d_{yz} bands (see the SI), although a limited accuracy of its experimental values impedes a quantitative analysis on this point.

Finally, we will analyze the disorder experienced by the charge carriers. Figure 4b presents the QP peak in the vicinity of E_F, whose $A(\omega,\mathbf{k}=\mathbf{k}_F)$ was obtained as EDCs integrated within ± 0.1 Å^{-1} around k_F of the d_{yz} bands. In this case the band-dispersion effects are minimized and, within the Fermi liquid paradigm, the spectral broadening due to electron–electron interaction vanishes at E_F. Therefore, the QP peak broadening (ΔE), which, neglecting the experimental energy resolution, is inversely proportional to the coherence length of the charge carriers, reflects the effective disorder they experience. In comparison with the LAO/STO's value $\Delta E \approx$ 62 meV, for the GAO/STO samples we observe $\Delta E \approx 50$ meV, which is close to the resolution limit of ~40 meV of our experiment. The reduced ΔE expresses the smaller effective disorder experienced by the d_{yz}-derived charge.

DISCUSSION

Effect of the Band Order on μ_e. The central question now is, how does the observed band-order anomaly affect μ_e? Figure 1 sketches the distribution of the V_Os relative to the depopulated d_{xy} and populated d_{xz}/d_{yz} electron density in GAO/STO. The V_Os effectively diffuse to the top STO layer, reducing their concentration and thereby the associated defect scattering in the deeper STO region.[12] This reduction is confirmed by our analysis of the QP peak width from the $d_{xz}/$

d_{yz} electrons extending into this region, which has evidenced a small effective disorder experienced by these electrons compared to LAO/STO. Located in the defect-free region, the d_{xz}/d_{yz} electrons deliver high $\mu_e^{xz/yz}$, whereas the d_{xy} states, located in the defect-rich top layer,[4,13,21] are depopulated and thus do not poison the overall μ_e. This interplay between the spatial distribution and population of the electron states is the main driving force behind the boost of μ_e in GAO/STO. Obviously, the boost critically depends on the spatial distribution of the V_O and other defect sites, highly sensitive to the sample growth and annealing protocol.[12]

The $d_{xy} > d_{xz}/d_{yz}$ band order will affect virtually all the properties of the GAO/STO besides μ_e. For example, it should reverse the sign of the gating voltage corresponding to the Lifshitz transition, where the crossover from the one-band to multi-band regime causes dramatic changes in physical properties of the STO-based heterostructures, including the superconducting transition temperature, electron pairing strength, and spin–orbit coupling.[39] Moreover, our ARPES findings may also have implications for the mechanism of superconductivity in GAO/STO, as this phenomenon in the STO-based systems is usually observed in the multi-band conduction regime.[40] Both points still await experimental verification, though.

Depth Extension of the 2DES. The connection of the ARPES data to the carrier density is established by the Luttinger theorem.[41] For the 2D systems, it states that n_s is equal to the sum of the partial Luttinger counts, $2 \int_{FS} \frac{d^2k}{(2\pi)^2}$, over all sheets constituting the FS. However, the application of this theorem to our case is not straightforward, even knowing the experimental FS of GAO/STO (see the SI). First, a typical feature of the STO-based systems is the electronic phase separation, where conducting regions co-exist with insulating ones.[18,42,43] While the experimental FS reflects the local electron density in the conducting areas, the integral n_s can be smaller. Second, if the interfacial $V(\mathbf{r})$ is sufficiently long-range, it hosts a ladder of quantum-well (QW) states,[44] and the Luttinger count should include the FS sheets through all of them. However, whereas the first QW state is located close to the interface, the higher-order ones are shifted deeper into the STO bulk,[45] where they can escape detection within the probing depth of the ARPES experiment while contributing to the total n_s. Because of the missing higher-order FS sheets, the Luttinger count of the FS apparent in ARPES may under-estimate the n_s measured in transport.

Intriguingly, the experimental $\mathbf{k}_F$ values found by ARPES for GAO/STO show an increase of the corresponding Luttinger counts by only ~15% between the low- and high-n_s samples, which is much less compared to the increase of transport n_s by a factor of ~20. This discrepancy may manifest the two effects discussed above. First, the lateral increase of the conducting phase between the low- and high-n_s samples, estimated from intensity of the 2DES signal as described in ref 18, measures ~70%. The remaining contribution to the n_s increase of more than an order of magnitude should then manifest a long-range $V(\mathbf{r})$ in the high-n_s sample, which supports an electron-density accumulation in higher-order d_{xz}/d_{yz}-derived QW states located in STO beyond the top 2–3 u.c. reached by ARPES. This situation can be viewed as a transformation of the 2DES into a quasi-three-dimensional system expanding deep into V_O-free STO. In this case, the increase of n_s should be associated with an increase of μ_e, and it indeed increases by a factor of ~8

between our samples. This physical picture resolves the long-standing puzzle why GAO/STO denies the "small n_s–large μ_e" paradigm often advocated for oxide interfaces, although other cases have been reported where this paradigm was violated by similar dimensionality transformations.[46]

Effects of the EPI. The weakening of the EPI, expressed by the Z_0 values in Figure 4a, is another aspect of GAO/STO contributing to the μ_e-boost. For many systems, such weakening is caused by screening of the EPI by mobile electrons. In our case, however, ARPES shows that, at least near the interface, the d_{xz}/d_{yz}-derived electron density in GAO/STO is smaller than the d_{xz}/d_{yz} (and all the more $d_{xy} + d_{xz}/d_{yz}$) density in our LAO/STO. In fact, the EPI may be amplified by trapping (localization) of charge carriers on defects[47] or via more exotic Anderson localization.[48] This lowers the crystal symmetry, allowing otherwise prohibited phonon modes and thus additional EPI channels. The involvement of such localization-enhanced EPI in our case is evident from the phonon-mode continuum displayed by LAO/STO's $A(\omega)$ as opposed to the single mode in GAO/STO. Then the reduction of the effective defect concentration in GAO/STO, expressed by the smaller disorder seen in the QP-peak width, Figure 4b, explains the reduction of the EPI. This effect traces back, again, to the band-order anomaly that shifts the total 2DES into the V_O-free bulk of STO. The small but significant decrease of EPI in the high-n_s GAO/STO sample compared to the low-n_s one should be a combined effects of smaller effective disorder due to the deeper expansion of the 2DES into STO and of larger n_s screening the EPI.

The observed weakening of EPI in GAO/STO propagates into μ_e not only by polaronic renormalization of the electron effective mass but also by mediating electron scattering on defects, which can somehow be viewed as frozen phonons. Therefore, the defects affect μ_e not only through their concentration but also through the EPI-mediated electron-defect scattering strength which, in turn, increases with the defect concentration. This cumulative effect results in a steep non-linear change of μ_e as a function of the latter, predicted within the mean-field approximation already four decades ago[49] and later reproduced by approximation-free diagrammatic Monte Carlo calculations.[50−52] This effect is likely to be at play to boost μ_e as the effective V_O concentration experienced by the d_{xz}/d_{yz} electrons in GAO/STO decreases thanks to the band-order anomaly. Indeed, this decrease is evident from our analysis of the QP peak width in Figure 4b. The tendency of V_Os to cluster[18] can also affect μ_e.

CONCLUSIONS AND OUTLOOK

To summarize our results, we have found that the $\mathbf{k}$-resolved electronic structure of the 2DES at the GAO/STO interface stands out among all other known STO-based interfaces in terms of the band order. The upward shift of the d_{xy} states with respect to the d_{xz}/d_{yz} ones, forming the anomalous $d_{xy} > d_{xz}/d_{yz}$ band order and depopulating the d_{xy} band, is attributed to a change in the CF configuration around the Ti ions as the spinel–perovskite GAO/STO interface breaks the perovskite lattice symmetry. The band order affects most physical properties of GAO/STO, and in the first place boosts μ_e of the interfacial 2DES, which shifts away from the defect-rich interface toward the STO bulk.

The μ_e boost at the GAO/STO interface appears as a multi-faceted phenomenon, identifying three routes to design high-mobility oxide devices in general:

(1) The static defects, in particular the V_Os, affect μ_e through low-temperature electron scattering. With inspiration from the semiconductor HEMTs, this scattering can be reduced by shifting the depth profile of V_Os away from that of the 2DES to minimize their overlap. In GAO/STO this is achieved by the accumulation of the V_Os at the top TiO_2 layer of STO, away from the 2DES located deeper in STO.[12] The crucial role of this *defect-engineering* route for GAO/STO can be assessed by varying the growth protocol and thus distribution of V_Os.[53]

(2) This work suggests the second route, *band-order engineering*. Complementary to defect engineering, this route allows control over the 2DES depth profile in order to shift it away from the V_Os. In GAO/STO this is achieved with the $d_{xy} > d_{xz}/d_{yz}$ band order, which depopulates the d_{xy} states and leaves only the d_{xz}/d_{yz} electrons, located deeper in the STO bulk compared to the d_{xy} ones in the defect-rich top layer. Moreover, the increase of n_s in GAO/STO expands the 2DES into the STO bulk and thus further increases μ_e. The band order can be manipulated through the CF, driven by the interface-symmetry breaking and, in addition, tuned by doping, such as substituting Al^{3+} ions in GAO with those of a dissimilar valence state.

(3) The third way to boost μ_e is the *EPI-engineering* route that invokes the EPI-mediated electron interaction with the defects. As the EPI itself is enhanced by electron trapping on the defects, the resulting μ_e shows a steep non-linear dependence of their effective concentration, in our case that of the V_Os over the 2DES spatial extension. In this context, the EPI-engineering route is intimately connected with the defect and band-order engineering. The EPI can also be tuned through n_s varied, for example, by electrostatic gating.[54] Thereby, the GAO/STO interface teaches us a triad of interconnected routes—defect, band-order, and EPI-engineering—toward realization of a high-mobility "oxide HEMT". None of them alone but only the whole triad, and perhaps assisted by other yet unknown mechanisms, can exhaust the entire μ_e boost in GAO/STO of more than 2 orders compared to the paradigm LAO/STO heterostructures.

In a broader perspective, the crucial role of the band-order engineering extends from merely electron transport toward the whole world of other exotic properties of the oxide systems, including gate-tunable superconductivity, Lifshitz transition, electron pairing without superconductivity, spin–orbit coupling, magnetic ordering, *etc.* For example, the $d_{xy} > d_{xz}/d_{yz}$ band order observed in GAO/STO should revert the gate-voltage sign of the Lifshitz transition as well as switch the superconductivity from the multi-band to one-band regime. Our work puts forward a prospect to change the band order through appropriate lattice-symmetry breaking and tuning the CF splitting by dopants of a dissimilar valence state or by (pseudo)epitaxial growth of other members of the large spinel crystal family. Our findings motivate the search for other oxide interfacial pairs, where the d_{xy} bands totally depopulate to maximize μ_e, using modern big-data computational methods.

METHODS

Sample Fabrication and Characterization. The samples were manufactured by pulsed laser deposition (PLD) on STO substrates. The reference LAO/STO samples were grown in slightly oxygen-deficient conditions and annealed in oxygen *ex situ*, following the protocol described in refs 18 and 19. The GAO/STO samples were manufactured using the protocol described elsewhere[16] under an oxygen partial pressure varied from 4×10^{-6} to 8×10^{-6} mbar in order to change the transport properties through the V_O concentration. The two investigated GAO/STO samples were metallic, with low $n_s \approx 3 \times 10^{13}$ cm^{-2} and high $n_s \approx 6 \times 10^{14}$ cm^{-2} at room temperature, with the residual resistance ratio $R_s(300\ K)/R_s(2\ K) \approx 1100$ and 9300, respectively. The high residual resistance ratios are the hallmarks of samples with high low-temperature μ_e values,[16] which were $\sim$12 000 and 100 000 cm^2/(V·s) at 2 K for the two samples.

ARPES Experiment. The experiments were performed at the soft-X-ray ARPES facility[55] installed at the ADRESS beamline[56] of the Swiss Light Source, Paul Scherrer Institute, Switzerland. Variable X-ray polarization delivered by this beamline allowed symmetry analysis of the electron states. The FS maps were recorded at a combined (beamline plus analyzer PHOIBOS-150) energy resolution of $\sim$60 meV, and $E(\mathbf{k})$ maps at $\sim$40 meV. Angular resolution of the analyzer was $\sim$0.1°. The sample was cooled down to $\sim$12 K in order to quench the relaxation of $\mathbf{k}$-conservation due to the thermal motion of the atoms. The photon flux was $\sim$10^{13} photons/s and focused into a spot of $30 \times 75\ \mu m^2$ on the sample surface. Other relevant experimental details are reported elsewhere.[6,19]

During the ARPES data acquisition, the strength of the 2DES signal from our LAO/STO and GAO/STO samples gradually increased because the V_Os generated under X-ray irradiation injected mobile electrons into the 2DES.[18,19] However, the observed band dispersions and population stayed constant, following the electronic phase separation scenario typical of the STO-based systems.[18,20,42,43] The irradiation-induced increase of the 2DES signal from the high-n_s GAO/STO sample was smaller compared to the low-n_s one. All reported ARPES data were acquired after an irradiation time of more than 1 h to ensure saturation. The experimental resonant-photoemission intensity maps as a function of $h\nu$ through the Ti L-edge for our LAO/STO and low-n_s GAO/STO samples are presented in the SI. The intensity of the V_O-derived IG states at a binding energy around -1.2 eV and of the 2DES states near E_F sharply varied with $h\nu$. The data in given the main text were acquired at the L_3 resonance at $h\nu = 460.4$ eV, where the d_{xy}-to-d_{xz}/d_{yz} intensity ratio enhances compared to the L_2 resonance.[6,19] The corresponding FS maps of GAO/STO measured at different X-ray polarizations are presented in the SI. Besides the reduced FS area, their notable difference compared to the FS maps of LAO/STO is the streaks of intensity stretching between the Γ points. This peculiarity might be related to linear clusters of the interfacial V_Os or, although scanning-SQUID measurements on similarly prepared samples have found micrometer-size domains, the existence of domains whose size would be below the coherence length of the ARPES experiment (for details see the SI).

ASSOCIATED CONTENT

Ⓢ **Supporting Information**

The Supporting Information is available free of charge at https://pubs.acs.org/doi/10.1021/acsnano.0c07609.

Ti L-edge resonant photoemission data, effective-mass analysis, DFT calculations, and experimental Fermi surface (PDF)

AUTHOR INFORMATION

Corresponding Authors

Nini Pryds — *Department of Energy Conversion and Storage, Technical University of Denmark, 2800 Kgs. Lyngby, Denmark;* Ⓞ orcid.org/0000-0002-5718-7924; Email: nipr@dtu.dk

Vladimir N. Strocov — *Swiss Light Source, Paul Scherrer Institute, 5232 Villigen-PSI, Switzerland;* Ⓞ orcid.org/0000-0002-1147-8486; Email: vladimir.strocov@psi.ch

Authors

Alla Chikina − *Swiss Light Source, Paul Scherrer Institute, 5232 Villigen-PSI, Switzerland; Institute of Physics and Astronomy, Aarhus University, 8000 Aarhus, Denmark;* ⓞ orcid.org/0000-0003-3635-6503

Dennis V. Christensen − *Department of Energy Conversion and Storage, Technical University of Denmark, 2800 Kgs. Lyngby, Denmark*

Vladislav Borisov − *Institut für Theoretische Physik, Goethe-Universität Frankfurt am Main, 60438 Frankfurt am Main, Germany; Department of Physics and Astronomy, Uppsala University, 5120 Uppsala, Sweden*

Marius-Adrian Husanu − *Swiss Light Source, Paul Scherrer Institute, 5232 Villigen-PSI, Switzerland; National Institute of Materials Physics, 077125 Magurele, Romania;* ⓞ orcid.org/0000-0003-4510-6653

Yunzhong Chen − *Department of Energy Conversion and Storage, Technical University of Denmark, 2800 Kgs. Lyngby, Denmark; Beijing National Laboratory for Condensed Matter Physics, Institute of Physics, Chinese Academy of Sciences, Beijing 100190, China;* ⓞ orcid.org/0000-0001-8368-5823

Xiaoqiang Wang − *Swiss Light Source, Paul Scherrer Institute, 5232 Villigen-PSI, Switzerland*

Thorsten Schmitt − *Swiss Light Source, Paul Scherrer Institute, 5232 Villigen-PSI, Switzerland*

Milan Radovic − *Swiss Light Source, Paul Scherrer Institute, 5232 Villigen-PSI, Switzerland*

Naoto Nagaosa − *RIKEN Center for Emergent Matter Science, Wako, Saitama 351-0198, Japan; Department of Applied Physics, University of Tokyo, Tokyo 113-8656, Japan*

Andrey S. Mishchenko − *RIKEN Center for Emergent Matter Science, Wako, Saitama 351-0198, Japan*

Roser Valentí − *Institut für Theoretische Physik, Goethe-Universität Frankfurt am Main, 60438 Frankfurt am Main, Germany*

Complete contact information is available at:
https://pubs.acs.org/10.1021/acsnano.0c07609

Author Contributions

A.C., D.V.C., Y.C., M.-A.H., M.R., N.P., and V.N.S. performed the ARPES experiment, assisted by X.W. and T.S. V.N.S., A.C., and M.-A.H. processed the ARPES data. D.V.C. and Y.C., supported by N.P., fabricated the samples and performed their transport characterization. V.N.S. and N.P. conceived the idea of the band-order effect on electron mobility, and A.S.M., supported by N.N., elaborated the physics of EPI. V.B., supported by R.V., performed the CF calculations. V.N.S. wrote the manuscript, with contributions from A.C., D.V.C., V.B., and A.S.M. All authors discussed the results, interpretations, and scientific concepts.

Notes

The authors declare no competing financial interest.

REFERENCES

(1) Hwang, H. Y.; Iwasa, Y.; Kawasaki, M.; Keimer, B.; Nagaosa, N.; Tokura, Y. Emergent Phenomena at Oxide Interfaces. *Nat. Mater.* **2012**, *11*, 103−113.

(2) Mannhart, J.; Schlom, D. G. Oxide Interfaces - An Opportunity for Electronics. *Science* **2010**, *327* (5973), 1607−1611.

(3) Bert, J. A.; Kalisky, B.; Bell, C.; Kim, M.; Hikita, Y.; Hwang, H. Y.; Moler, K. A. Direct Imaging of the Coexistence of Ferromagnetism and Superconductivity at the LaAlO₃/SrTiO₃ Interface. *Nat. Phys.* **2011**, *7*, 767−771.

(4) Gariglio, S.; Reyren, N.; Caviglia, A. D.; Triscone, J.-M. Superconductivity at the LaAlO₃/SrTiO₃ Interface. *J. Phys.: Condens. Matter* **2009**, *21*, 164213.

(5) Sulpizio, J. A.; Ilani, S.; Irvin, P.; Levy, J. Nanoscale Phenomena in Oxide Heterostructures. *Annu. Rev. Mater. Res.* **2014**, *44*, 117−149.

(6) Cancellieri, C.; Mishchenko, A. S.; Aschauer, U.; Filippetti, A.; Faber, C.; Barišić, O. S.; Rogalev, V. A.; Schmitt, T.; Nagaosa, N.; Strocov, V. N. Polaronic Metal State at the LaAlO₃/SrTiO₃ Interface. *Nat. Commun.* **2016**, *7*, 10386.

(7) Mimura, T. The Early History of the High Electron Mobility Transistor (HEMT). *IEEE Trans. Microwave Theory Tech.* **2002**, *50*, 780−782.

(8) Lev, L. L.; Maiboroda, I. O. -A.; Husanu, M.; Grichuk, E. S.; Chumakov, N. K.; Ezubchenko, I. S.; Chernykh, I. A.; Wang, X.; Tobler, B.; Schmitt, T.; Zanaveskin, M. L.; Valeyev, V. G.; Strocov, V. N. **k**-Space Imaging of Anisotropic 2D Electron Gas in GaN/GaAlN High-Electron-Mobility Transistor Heterostructures. *Nat. Commun.* **2018**, *9*, 2653.

(9) Chen, Y. Z.; Trier, F.; Wijnands, T.; Green, R. J.; Gauquelin, N.; Egoavil, R.; Christensen, D. V.; Koster, G.; Huijben, M.; Bovet, N.; Macke, S.; He, F.; Sutarto, R.; Andersen, N. H.; Sulpizio, J. A.; Honig, M.; Prawiroatmodjo, G. E. D. K.; Jespersen, T. S.; Linderoth, S.; Ilani, S.; et al. Extreme Mobility Enhancement of Two-Dimensional Electron Gases at Oxide Interfaces by Charge-Transfer-Induced Modulation Doping. *Nat. Mater.* **2015**, *14*, 801−806.

(10) Chen, Y. Z.; Bovet, N.; Trier, F.; Christensen, D. V.; Qu, F. M.; Andersen, N. H.; Kasama, T.; Zhang, W.; Giraud, R.; Dufouleur, J.; Jespersen, T. S.; Sun, J. R.; Smith, A.; Nygård, J.; Lu, L.; Büchner, B.; Shen, B. G.; Linderoth, S.; Pryds, N. A High-Mobility Two-Dimensional Electron Gas at the Spinel/Perovskite Interface of γ-Al₂O₃/SrTiO₃. *Nat. Commun.* **2013**, *4*, 1371.

(11) Falson, J.; Kozuka, Y.; Uchida, M.; Smet, J. H.; Arima, T.-H.; Tsukazaki, A.; Kawasaki, M. MgZnO/ZnO Heterostructures with Electron Mobility Exceeding 1 × 10⁶ cm²/Vs. *Sci. Rep.* **2016**, *6*, 26598.

(12) Schütz, P.; Christensen, D. V.; Borisov, V.; Pfaff, F.; Scheiderer, P.; Dudy, L.; Zapf, M.; Gabel, J.; Chen, Y. Z.; Pryds, N.; Rogalev, V. A.; Strocov, V. N.; Schlueter, C.-L.; Lee, T.; Jeschke, H. O.; Valentí, R.; Sing, M.; Claessen, R. Microscopic Origin of the Mobility Enhancement at a Spinel/Perovskite Oxide Heterointerface Revealed by Photoemission Spectroscopy. *Phys. Rev. B: Condens. Matter Mater. Phys.* **2017**, *96*, 161409.

(13) Delugas, P.; Filippetti, A.; Fiorentini, V.; Bilc, D. I.; Fontaine, D.; Ghosez, P. Spontaneous 2-Dimensional Carrier Confinement at the *N*-Type SrTiO₃/LaAlO₃ Interface. *Phys. Rev. Lett.* **2011**, *106*, 166807.

(14) Cao, Y.; Liu, X.; Shafer, P.; Middey, S.; Meyers, D.; Kareev, M.; Zhong, Z.; Kim, J.-W.; Ryan, P. J.; Arenholz, E.; Chakhalian, J. Anomalous Orbital Structure in a Spinel-Perovskite Interface. *npj Quantum Materials.* **2016**, *1*, 166807.

(15) Mardegan, J. R. L.; Christensen, D. V.; Chen, Y. Z.; Parchenko, S.; Avula, S. R. V.; Ortiz-Hernandez, N.; Decker, M.; Piamonteze, C.; Pryds, N.; Staub, U. Magnetic and Electronic Properties at the γ-

Al$_2$O$_3$/SrTiO$_3$ Interface. *Phys. Rev. B: Condens. Matter Mater. Phys.* **2019**, *99*, 134423.

(16) Christensen, D. V.; Frenkel, Y.; Schütz, P.; Trier, F.; Wissberg, S.; Claessen, R.; Kalisky, B.; Smith, A.; Chen, Y. Z.; Pryds, N. Electron Mobility in γ-Al$_2$O$_3$/SrTiO$_3$. *Phys. Rev. Appl.* **2018**, *9*, 7927.

(17) Niu, W.; Zhang, Y.; Gan, Y.; Christensen, D. V.; Soosten, M. V.; Garcia-Suarez, E. J.; Riisager, A.; Wang, X.; Xu, Y.; Zhang, R.; Pryds, N.; Chen, Y. Giant Tunability of the Two-Dimensional Electron Gas at the Interface of γ-Al$_2$O$_3$/SrTiO$_3$. *Nano Lett.* **2017**, *17*, 6878−6885.

(18) Strocov, V. N.; Chikina, A.; Caputo, M.-A.; Husanu, M.-A.; Bisti, F.; Bracher, D.; Schmitt, T.; Miletto Granozio, F.; Vaz, C. A. F.; Lechermann, F. Electronic Phase Separation at LaAlO$_3$/SrTiO$_3$ Interfaces Tunable by Oxygen Deficiency. *Physical Review Materials.* **2019**, *3*, 106001.

(19) Chikina, A.; Lechermann, F.; Husanu, M.-A.; Caputo, M.; Cancellieri, C.; Wang, X.; Schmitt, T.; Radovic, M.; Strocov, V. N. Orbital Ordering of the Mobile and Localized Electrons at Oxygen-Deficient LaAlO$_3$/SrTiO$_3$ Interfaces. *ACS Nano* **2018**, *12*, 7927−7935.

(20) Strocov, V. N. Photoemission Response of 2D Electron States. *J. Electron Spectrosc. Relat. Phenom.* **2018**, *229*, 100−107.

(21) Cancellieri, C.; Reinle-Schmitt, M. L.; Kobayashi, M.; Strocov, V. N.; Willmott, P. R.; Fontaine, D.; Ghosez, P.; Filippetti, A.; Delugas, P.; Fiorentini, V. Doping-Dependent Band Structure of LaAlO$_3$/SrTiO$_3$ Interfaces by Soft X-Ray Polarization-Controlled Resonant Angle-Resolved Photoemission. *Phys. Rev. B: Condens. Matter Mater. Phys.* **2014**, *89*, 121412.

(22) Strocov, V. N.; Cancellieri, C.; Mishchenko, A. S. Electrons and Polarons at Oxide Interfaces Explored by Soft-X-Ray ARPES. In *Spectroscopy of Complex Oxide Interfaces: Photoemission and Related Spectroscopies*; Springer Series in Materials Science *266*; Springer: Cham, 2018, 107−151.

(23) Cancellieri, C., Strocov, V. N., Eds. *Spectroscopy of Complex Oxide Interfaces: Photoemission and Related Spectroscopies*; Springer Series in Materials Science *266*; Springer: Cham, 2018.

(24) Trier, F.; Amoruso, S.; Christensen, D. V.; Sambri, A.; Chen, Y. Z.; Wang, X.; Stamate, E.; Bruzzese, R.; Pryds, N. Controlling the Conductivity of Amorphous LaAlO$_3$/SrTiO$_3$ Interfaces by *in Situ* Application of an Electric Field during Fabrication. *Appl. Phys. Lett.* **2013**, *103*, 031607.

(25) Li, C.; Hong, Y.; Xue, H.; Wang, X.; Li, Y.; Liu, K.; Jiang, W.; Liu, M.; He, L.; Dou, R.; Xiong, C.; Nie, J. Formation of Two-Dimensional Electron Gas at Amorphous/Crystalline Oxide Interfaces. *Sci. Rep.* **2018**, *8*, 404.

(26) Chikina, A.; Caputo, M.; Naamneh, M.; Christensen, D. V.; Schmitt, T.; Radovic, M.; Strocov, V. N. Semiconductors: X-Ray Writing of Metallic Conductivity and Oxygen Vacancies at Silicon/SrTiO$_3$ Interfaces. *Adv. Funct. Mater.* **2019**, *29*, 1970172.

(27) Rödel, T. C.; Fortuna, F.; Sengupta, S.; Frantzeskakis, E.; Le Fèvre, P.; Bertran, F.; Mercey, B.; Matzen, S.; Agnus, G.; Maroutian, T.; Lecoeur, P.; Santander-Syro, A. F. Universal Fabrication of 2D Electron Systems in Functional Oxides. *Adv. Mater.* **2016**, *28*, 1976−1980.

(28) Kormondy, K. J.; Gao, L.; Li, X.; Lu, S.; Posadas, A. B.; Shen, S.; Tsoi, M.; McCartney, M. R.; Smith, D. J.; Zhou, J.; Lev, L. L.; Husanu, M.-A.; Strocov, V. N.; Demkov, A. A. Large Positive Linear Magnetoresistance in the Two-Dimensional t_{2g} Electron Gas at the EuO/SrTiO$_3$ Interface. *Sci. Rep.* **2018**, *8*, 7771.

(29) Posadas, A. B.; Kormondy, K. J.; Guo, W.; Ponath, P.; Geler-Kremer, J.; Hadamek, T.; Demkov, A. A. Scavenging of Oxygen from SrTiO$_3$ during Oxide Thin Film Deposition and the Formation of Interfacial 2DEGs. *J. Appl. Phys.* **2017**, *121*, 105302.

(30) Sing, M.; Jeschke, H. O.; Lechermann, F.; Valentí, R.; Claessen, R. Influence of Oxygen Vacancies on Two-Dimensional Electron Systems at SrTiO$_3$-Based Interfaces and Surfaces. *Eur. Phys. J.: Spec. Top.* **2017**, *226*, 2457−2475.

(31) Plumb, N. C.; Salluzzo, M.; Razzoli, E.; Månsson, M.; Falub, M.; Krempasky, J.; Matt, C. E.; Chang, J.; Schulte, M.; Braun, J.;

Ebert, H.; Minár, J.; Delley, B.-J.; Zhou, K.; Schmitt, T.; Shi, M.; Mesot, J.; Patthey, L.; Radović, M. Mixed Dimensionality of Confined Conducting Electrons in the Surface Region of SrTiO$_3$. *Phys. Rev. Lett.* **2014**, *113*, 086801.

(32) Wang, Z.; McKeown Walker, S.; Tamai, A.; Wang, Y.; Ristic, Z.; Bruno, F. Y.; de la Torre, A.; Riccò, S.; Plumb, N. C.; Shi, M.; Hlawenka, P.; Sánchez-Barriga, J.; Varykhalov, A.; Kim, T. K.; Hoesch, M.; King, P. D. C.; Meevasana, W.; Diebold, U.; Mesot, J.; Moritz, B.; et al. Tailoring the Nature and Strength of Electron-Phonon Interactions in the SrTiO$_3$(001) 2D Electron Liquid. *Nat. Mater.* **2016**, *15*, 835−839.

(33) Laukhin, V.; Copie, O.; Rozenberg, M. J.; Weht, R.; Bouzehouane, K.; Reyren, N.; Jacquet, E.; Bibes, M.; Barthélémy, A.; Herranz, G. Electronic Subband Reconfiguration in ad0-Perovskite Induced by Strain-Driven Structural Transformations. *Phys. Rev. Lett.* **2012**, *109*, 226601.

(34) Herranz, G.; Singh, G.; Bergeal, N.; Jouan, A.; Lesueur, J.; Gázquez, J.; Varela, M.; Scigaj, M.; Dix, N.; Sánchez, F.; Fontcuberta, J. Engineering Two-Dimensional Superconductivity and Rashba Spin-Orbit Coupling in LaAlO$_3$/SrTiO$_3$ Quantum Wells by Selective Orbital Occupancy. *Nat. Commun.* **2015**, *6*, 6028.

(35) Straub, Th.; Claessen, R.; Steiner, P.; Hüfner, S.; Eyert, V.; Friemelt, K.; Bucher, E. Many-Body Definition of a Fermi Surface: Application to Angle-Resolved Photoemission. *Phys. Rev. B: Condens. Matter Mater. Phys.* **1997**, *55*, 13473.

(36) Salluzzo, M.; Cezar, J. C.; Brookes, N. B.; Bisogni, V.; De Luca, G. M.; Richter, C.; Thiel, S.; Mannhart, J.; Huijben, M.; Brinkman, A.; Rijnders, G.; Ghiringhelli, G. Orbital Reconstruction and the Two-Dimensional Electron Gas at the LaAlO$_3$/SrTiO$_3$ Interface. *Phys. Rev. Lett.* **2009**, *102*, 166804.

(37) Zabaleta, J.; Borisov, V. S.; Wanke, R.; Jeschke, H. O.; Parks, S. C.; Baum, B.; Teker, A.; Harada, T.; Syassen, K.; Kopp, T.; Pavlenko, N.; Valentí, R.; Mannhart, J. Hydrostatic Pressure Response of an Oxide-Based Two-Dimensional Electron System. *Phys. Rev. B: Condens. Matter Mater. Phys.* **2016**, *93*, 235117.

(38) Krsnik, J.; Strocov, V. N.; Nagaosa, N.; Barisic, O. S.; Rukelj, Z.; Yakubenya, S. M.; Mishchenko, A. S. Manifestation of the Electron-Phonon Interaction Range in the Angle Resolved Photoemission Spectra. *Phys. Rev. B: Condens. Matter Mater. Phys.* **2020**, *102*, 121108.

(39) Joshua, A.; Pecker, S.; Ruhman, J.; Altman, E.; Ilani, S. A Universal Critical Density Underlying the Physics of Electrons at the LaAlO$_3$/SrTiO$_3$ Interface. *Nat. Commun.* **2012**, *3*, 1129.

(40) Gan, Y.; Christensen, D. V.; Zhang, Y.; Zhang, H.; Krishnan, D.; Zhong, Z.; Niu, W.; Carrad, D. J.; Norrman, K.; von Soosten, M.; Jespersen, T. S.; Shen, B.; Gauquelin, N.; Verbeeck, J.; Sun, J.; Pryds, N.; Chen, Y. Diluted Oxide Interfaces with Tunable Ground States. *Adv. Mater.* **2019**, *31*, 1805970.

(41) Luttinger, J. M. Fermi Surface and Some Simple Equilibrium Properties of a System of Interacting Fermions. *Phys. Rev.* **1960**, *119*, 1153.

(42) Scopigno, N.; Bucheli, D.; Caprara, S.; Biscaras, J.; Bergeal, N.; Lesueur, J.; Grilli, M. Phase Separation from Electron Confinement at Oxide Interfaces. *Phys. Rev. Lett.* **2016**, *116*, 026804.

(43) Dudy, L.; Sing, M.; Scheiderer, P.; Denlinger, J. D.; Schütz, P.; Gabel, J.; Buchwald, M.; Schlueter, C.; Lee, T.-L.; Claessen, R. *In Situ* Control of Separate Electronic Phases on SrTiO$_3$ Surfaces by Oxygen Dosing. *Adv. Mater.* **2016**, *28*, 7443−7449.

(44) King, P. D. C.; McKeown Walker, S.; Tamai, A.; de la Torre, A.; Eknapakul, T.; Buaphet, P.; Mo, S.-K.; Meevasana, W.; Bahramy, M. S.; Baumberger, F. Quasiparticle Dynamics and Spin-Orbital Texture of the SrTiO$_3$ Two-Dimensional Electron Gas. *Nat. Commun.* **2014**, *5*, 3414.

(45) Biscaras, J.; Hurand, S.; Feuillet-Palma, C.; Rastogi, A.; Budhani, R. C.; Reyren, N.; Lesne, E.; Lesueur, J.; Bergeal, N. Limit of the Electrostatic Doping in Two-Dimensional Electron Gases of LaXO$_3$(X = Al, Ti)/SrTiO$_3$. *Sci. Rep.* **2015**, *4*, 6788.

(46) Herranz, G.; Basletić, M.; Bibes, M.; Carrétéro, C.; Tafra, E.; Jacquet, E.; Bouzehouane, K.; Deranlot, C.; Hamzić, A.-M.; Broto, J.; Barthélémy, A.; Fert, A. High Mobility in LaAlO$_3$/SrTiO$_3$

Heterostructures: Origin, Dimensionality, and Perspectives. *Phys. Rev. Lett.* **2007**, *98*, 216803.

(47) Mishchenko, A. S.; Nagaosa, N.; Alvermann, A.; Fehske, H.; De Filippis, G.; Cataudella, V.; Sushkov, O. P. Localization-Delocalization Transition of a Polaron near an Impurity. *Phys. Rev. B: Condens. Matter Mater. Phys.* **2009**, *79*, 180301.

(48) Pallecchi, I.; Telesio, F.; Li, D.; Fête, A.; Gariglio, S.; Triscone, J.-M.; Filippetti, A.; Delugas, P.; Fiorentini, V.; Marré, D. Giant Oscillating Thermopower at Oxide Interfaces. *Nat. Commun.* **2015**, *6*, 6678.

(49) Shinozuka, Y.; Toyozawa, Y. Self-Trapping in Mixed Crystal - Clustering, Dimensionality, Percolation. *J. Phys. Soc. Jpn.* **1979**, *46*, 505−514.

(50) de Candia, A.; De Filippis, G.; Cangemi, L. M.; Mishchenko, A. S.; Nagaosa, N.; Cataudella, V. Two-Channel Model for Optical Conductivity of High-Mobility Organic Crystals. *EPL (Europhysics Letters).* **2019**, *125*, 47002.

(51) De Filippis, G.; Cataudella, V.; Mishchenko, A. S.; Nagaosa, N.; Fierro, A.; de Candia, A. Crossover from Super- to Subdiffusive Motion and Memory Effects in Crystalline Organic Semiconductors. *Phys. Rev. Lett.* **2015**, *114*, 086601.

(52) Mishchenko, A. S.; Pollet, L.; Prokof'ev, N. V.; Kumar, A.; Maslov, D. L.; Nagaosa, N. Polaron Mobility in the "Beyond Quasiparticles" Regime. *Phys. Rev. Lett.* **2019**, *123*, 076601.

(53) Trier, F.; Christensen, D. V.; Pryds, N. Electron Mobility in Oxide Heterostructures. *J. Phys. D: Appl. Phys.* **2018**, *51*, 293002.

(54) Boschker, H.; Richter, C.; Fillis-Tsirakis, E.; Schneider, C. W.; Mannhart, J. Electron-Phonon Coupling and the Superconducting Phase Diagram of the LaAlO$_3$-SrTiO$_3$ Interface. *Sci. Rep.* **2015**, *5*, 12309.

(55) Strocov, V. N.; Wang, X.; Shi, M.; Kobayashi, M.; Krempasky, J.; Hess, C.; Schmitt, T.; Patthey, L. Soft-X-Ray ARPES Facility at the ADRESS Beamline of the SLS: Concepts, Technical Realisation and Scientific Applications. *J. Synchrotron Radiat.* **2014**, *21* (Pt 1), 32−44.

(56) Strocov, V. N.; Schmitt, T.; Flechsig, U.; Schmidt, T.; Imhof, A.; Chen, Q.; Raabe, J.; Betemps, R.; Zimoch, D.; Krempasky, J.; Wang, X.; Grioni, M.; Piazzalunga, A.; Patthey, L. High-Resolution Soft X-Ray Beamline ADRESS at the Swiss Light Source for Resonant Inelastic X-Ray Scattering and Angle-Resolved Photoelectron Spectroscopies. *J. Synchrotron Radiat.* **2010**, *17*, 631−643.